the OCCC signature is metabolism-related, in particular glycogen-related genes, suggesting that OCCC has a distinct metabolic character among the ovarian carcinomas [8]. In this context, our next goal was to characterize the genes responsible for this unique expression profile and define the function of these genes, which may then provide the basis for development of targeted molecular therapy that is specific for OCCC. In this study, we have chosen to focus on a specific OCCC signature gene, hepatic nuclear factor-1β gene (*HNF-1β*).

HNF-1β is a homeodomain-containing transcription factor that shares >80% amino acid sequence of homeodomain [9] homology with HNF-1α. These proteins dimerize and bind to the same DNA sequence as homodimers or heterodimers, and are known to regulate the expression of multiple genes through direct or indirect mechanisms [9]. Clinically, *HNF-1* mutations are responsible for "maturity-onset diabetes of the young (MODY)," a specific type of diabetes characterized by pancreatic hypoplasia. Diabetes has been reported in 58% of *HNF-1β* mutation carriers [10]. HNF-1β has been implicated in the development of the pancreas and is thought to be an essential regulator of the transcriptional network that controls pancreatic morphogenesis and the differentiation of pancreatic endocrine cells [11].

Tsuchiya et al. recently reported that HNF-1β is overexpressed in OCCC. Although they identified an anti-apoptotic effect of this gene, the precise mechanism and biological significance of HNF-1β in OCCC are not yet clear [12]. We have shown that HNF-1β is not only a component of the OCCC signature [8], but also included in the intracellular signaling network demonstrated by pathway analysis, suggesting that this gene plays an important role in the biology of OCCC [13]. Therefore, using HNF-1β knockdown in OCCC cells and HNF-1β overexpression in non-OCCC cells, we report herein elucidation of how HNF-1β functionally plays a role in the unique biology of OCCC from multiple point of view including cell proliferation, glucose metabolism and gene expressions.

MATERIALS AND METHODS

Cell Lines and Cell Culture

The OCCC cell lines, RMG1 and RMG2, and the serous carcinoma cell line, Hey, were cultured in RPMI1640 (Nikken, Kyoto, Japan) supplemented with 10% FBS in a humidified atmosphere containing 5% CO_2 at 37°C, as previously described [8].

Stable Knockdown and Overexpression of the *HNF-1β* Gene

Two *HNF-1β*-targeting short hairpin RNAs (shRNA; clone IDs: V2LHS_204881 and V2LHS_196459) and a non-silencing control (clone ID: RHS4348) were purchased from the GIPZ lentiviral shRNAmir library (Thermo Fisher Scientific, Huntsville, AL). RMG2 cells were infected with lentiviruses using a standard protocol using puromycin as the selective marker. RMG2 cells stably transfected with clones V2LHS_204881 or V2LHS_196459 were designated as RMG2-HNFβ-sh1 and RMG2-HNF1β-sh2, respectively, while RMG2 cells transfected with the non-silencing control were designated as RMG2-control. HNF-1β-suppressed stable cells in RMG1 cell line were established using same method above and designated as RMG1-HNF1β-sh1 while non-silencing control cells were designed as RMG1-control. For HNF-1β-overexpressing cell line, an HNF-1β-expressing lentivirus was constructed using an entry vector, pENTR221, containing the HNF-1β cDNA (Cat. No. OHS4559-99857765a; Thermo Fisher Scientific), and a destination vector, pLenti6/V5-DEST, in a Gateway system (Invitrogen Japan, Tokyo, Japan). Hey cells were infected with the HNF-1β-expressing lentivirus and were selected with blasticidin (Hey-HNF1β). The Hey cells transfected with an empty lentiviral vector were used as a control (Hey-control).

RNA Extraction and Quantitative Real-Time Polymerase Chain Reaction (qRT-PCR)

Total RNA was isolated from cells at 80% confluency using the RNeasy Mini Kit (Qiagen, Tokyo, Japan). Quantitative RT-PCR (qRT-PCR) was performed with primers and probe specific for *HNF-1β* (Assay ID: Hs00172123_ml) and *SOD1* (Assay ID: Hs00533490_m1; Taqman Gene Expression Assays; Applied Biosystems, Foster City, CA). All other assays were designed using Roche Probefinder software at the Universal Probe Library Assay Design Center (https://www.roche-applied-science.com/sis/rtpcr/upl/index.jsp?id=UP030000). Primer and probe sequences are provided in Supplementary Table 1. The samples were analyzed using a LightCycler 480 Real-Time PCR system (Roche Diagnostics, Tokyo, Japan).

Protein Extraction and Western Blot Analysis

Protein extraction and Western blotting were performed as reported previously [13] using the following primary antibodies: anti-HNF-1β (1:200; Santa Cruz, CA), anti-CDKN1B (1:1000, BD Bioscience, Franklin Lakes, NJ), anti-CDKN1A (1:200; Santa Cruz, CA), anti-GLUT1 (1:2500, Abcam Plc, Cambridge, UK), and anti-β-Actin (1:5000, Abcam Plc). Horseradish peroxidase-linked secondary antibodies were as follows: anti-goat Ig for HNF-1β (1:10 000, DAKO, Glostrup, Denmark) and CDKN1A (1:3000, GE Healthcare, Buckinghamshire, UK), anti-mouse Ig for CDKN1B (1:1000, GE Healthcare) and GAPDH (1:1000, Santa Cruz, CA), anti-rabbit Ig for GLUT1 and β-actin (1:2500 and 1:10 000, respectively, GE Healthcare). Images were obtained using a ChemiDoc XRS Plus system (Bio-Rad Laboratories, Tokyo, Japan).

Proliferation Assays

Cells were seeded into 96-well (2.5×10^3 cells/well) tissue culture plates and incubated for 3 d. Cell numbers were counted at three consecutive time points using a WST-8 (Water Soluble Tetrazolium salts) assay kit, which is a modified MTT (3-(4,5-di-methylthiazol-2-yl)-2,5-diphenyltetrazolium bromide) assay (Nakalai tesque, Kyoto, Japan). WST-8 assay values were normalized using the WST-8 value at the initial time point (Day 0), and compared between the groups. Population doubling times (PDT) were calculated based on the slope angle of the linear regression model for the three time points. In addition to WST-8 assays, cell numbers were directly counted in sextuplicate using the Countess Automated cell counter (Invitrogen) after the cells were seeded into 6-well tissue culture plates (3.0×10^5 cells/well) and incubated for 2, 5, and 11 d. The values were normalized at the initial time point (Day 0) same as above.

The Cell Cycle Analysis

The cell cycle analysis was performed as described previously [14]. The cells (1×10^6/well) were seeded in 10 cm^2 tissue culture dishes and cultured. The next day, cells were treated by nocodazole (Sigma–Aldrich, St. Louis, MO) at a final concentration of 0.5 μg/mL. After incubation for 0, 12, 24 h, cells were fixed with 70% ethanol, stained with 25 μg/mL propidium iodide (Sigma–Aldrich) and analyzed by FACS-Calibur flow cytometry with Cell Quest software (Becton Dickson, Franklin Lakes, NJ). For analysis of S-phase cell, cells were pulse-labeled with 10 μM BrdU for 1 h, fixed with 70% ethanol, denatured, and stained with APC conjugated Anti-BrdU Antibody (Becton Dickson), according to manufacturer's instructions.

Glucose Uptake Assay and Measurement of Lactate Production

Glucose uptake assays were performed as reported previously [15]. In brief, cells were incubated with glucose-free medium with 1 μCi 2-deoxy-[^{3}H]-D-glucose for 60 min. The cells were then washed three times with ice-cold PBS, collected, and quantified using a liquid scintillation counter. Lactate production was evaluated by measuring the concentration in the medium after 24 h of incubation. The assay was performed in triplicate, repeated three times and all the values were normalized by total protein concentration.

Glycolytic Flux Measurement

Measurement of glycolytic flux was performed as reported previously [16]. In brief, 0.7–3.0×10^6 cells were plated in a 10 cm^2 dish. The medium was changed the following day to a low-glucose (4.25 mmol/L) medium, and 12 h later, D-[3-^{3}H] glucose (3.6 μCi) was added. Every 2 h, 400 μL of the medium was taken for perchloric acid precipitation. The supernatant was applied to DOWEX 1 × 8 200–400 MESH Cl resin (Sigma–Aldrich Japan) after dilution in sodium tetraborate. The assay was performed in triplicate, repeated three times and the values were normalized by total protein concentration.

Glucose Uptake After Knockdown of GLUT1 in RMG2 Cells

GLUT1-specific siRNAs (Gene Solution siRNA, Cat. No. SI03089401 and No. SI00089264; Qiagen, Valencia, CA) and a negative-control siRNA (AllStars Negative Control siRNA; Qiagen) were transfected into RMG2 cells using HiPerFect Transfection Reagent (Qiagen). After 48 h incubation for with the siRNAs, glucose uptake assays were performed as described above. To confirm downregulation of *GLUT1* expression, qRT-PCR and Western blotting were performed as described above.

Microarray Analysis

RNA preparation and microarray analysis were performed as described [8,13]. Genome set Human U133 Plus 2.0 chips (Affymetrix, Santa Clara, CA) were used and expression of HNF-1β-knockdown and non-silencing control cells were compared using replicate cell preparations (five replicates each for RMG2-HNF1β-sh1 and RMG2-HNF1β-sh2, ten replicates for the RMG2-control). The enrichment of the OCCC signature in control (non-silencing) cells versus HNF-1β-knockdown cells was evaluated using Gene Set Enrichment Analysis (http://www.broadinstitute.org/gsea/index.jsp; GSEA). GSEA is a tool to determine if a particular set of pre-defined genes is over- or under-represented in a given sample. Here, probe sets that were previously shown [8] to be upregulated ($n = 393$) and downregulated ($n = 44$) were analyzed in RMG2 cells following knockdown of HNF-1β using two independent shRNAs. Interpretation of output figures is described in detail in the GSEA website (http://www.broadinstitute.org/gsea/index.jsp). Bayesian binary regression 2.0 (http://data.genome.duke.edu/oncogene.php) was used to calculate the HNF-1β signature probability scores of cells, indicating transcriptional pathway activity of HNF-1β downstream genes. Published microarray dataset GSE6008 (consisting of data from 8 OCCC and 91 non-OCCC specimens) was obtained from the Gene Expression Omnibus (GEO) website (http://www.ncbi.nlm.nih.gov/geo/). The GSE2109 dataset was also obtained from the GEO website, and 16 OCCC and 184 non-OCCC (excluding borderline tumors) were used for this analysis. Cell lines used in the present study are listed in Supplementary Table 2.

Statistical Analysis

Differences between groups were assessed using two-tailed unpaired *t*-tests. Data are represented as mean ± standard deviation (SD). Statistical analysis was performed using GraphPad Prism 4 software (GraphPad Software, Inc., La Jolla, CA), and probability values below 0.05 were considered as significant.

RESULTS

Effect of HNF-1β Knockdown on In Vitro Cell Proliferation

Expression of *HNF-1β* mRNA in shRNA-transfected cells was evaluated using qRT-PCR. *HNF-1β* expression was significantly suppressed (% suppression is 87.3% in RMG2-HNF1β-sh1 ($P = 0.009$) and 71.6% in RMG2-HNF1β-sh2 ($P = 0.013$) compared with the RMG2-control cells (Figure 1A). Suppression of HNF-1β protein was also confirmed by Western blot (Figure 1A).

Silencing of HNF-1β was associated with an increase in cell proliferation in RMG2 cells as detected using WST-8 assays ($P < 0.01$; Figure 1B) and based on cell counts ($P < 0.0001$; Figure 1B). PDT of RMG2-HNF1β-sh1, RMG2-HNF1β-sh2, and RMG2-control cells were 27.2, 21.5, and 34.5 h, respectively, as assessed by WST-8 assays, and were 1.94, 1.43, and 2.37 d, respectively, based on direct cell counts.

The suppression of HNF-1β in another OCCC cells, RMG1 (% suppression was 72.8% in RMG1-HNF1β-sh1 ($P = 0.041$; Figure 2A)) also caused accelerated cell proliferation as compared to control cells ($P < 0.0001$; Figure 2B). PDT of RMG1-HNF1β-sh1 and RMG1-control cells by WST-8 assays were 41.9 and 65.2 h, respectively.

Effect of HNF-1β Knockdown on Cell Cycle Progression and the Expression of CDKN1A and CDKN1B

We evaluated cell cycle progression by using Nocodazole, which arrests cell cycle at G2/M phase. Non-silencing RMG2 cells were significantly retarded in the transition G1/S to G2/M phase after 12, 24 h incubation with Nocodazole, compared to HNF-1β-knockdown RMG2 cells (Figure 1C). In addition, the detection of BrdU incorporation revealed that the percentage of S-phase cell was significantly reduced in 19.9% in RMG2-control cells, compared with 29.1% in RMG2-HNF1β-sh1 and 28.9% in RMG2-HNF1β-sh2 (Figure 1D).

Since HNF-1β knockdown resulted in an increase in cell proliferation in RMG2 cells, we evaluated CDKN1A and CDKN1B expression in HNF-1β-knockdown and non-silencing RMG2 cells by Western blot. CDKN1B protein levels in both RMG2-HNF1β-sh1 and RMG2-HNF1β-sh2 were significantly repressed as compared with the RMG2-control cells (% suppressions were 61.9% and 81.8%, respectively; Figure 1E). CDKN1A protein levels were also suppressed in RMG2-HNF1β-knockdown cells compared with RMG2-control cells (% suppressions were 81.9% and 83.1%, respectively; Figure 1F).

Effect of HNF-1β Knockdown on Glucose Uptake, Glycolytic Flux, and Lactate Secretion

The rate of glucose uptake was measured using a scintillation counter and normalized to that of non-silencing control cells. Uptake of extracellular glucose was significantly decreased in HNF-1β-knockdown cells as compared to control cells (RMG2-HNF1β-sh1, 42.6 ± 6.56%, $P = 0.0019$; RMG2-HNF1β-sh2, 40.2 ± 5.29% $P = 0.0014$; Figure 3A).

To verify that HNF-1β promotes glycolytic activity, we further examined glycolytic flux, which was determined by measuring the rate per hour of conversion of ^{3}H-labeled glucose to H_2O through the glycolytic pathway (Figure 3B). Glycolytic flux was significantly decreased in HNF-1β-knockdown cells as compared to control cells (RMG2-HNF1β-sh1, 56.0 ± 8.78%, $P = 0.0012$; RMG2-HNF1β-sh2, 49.8 ± 2.56%, $P < 0.0001$; Figure 3B).

Lactate secretion into the culture media was also measured and was significantly suppressed in HNF-1β-knockdown cells (RMG2-HNF1β-sh1, 70.0 ± 6.46%, $P = 0.030$ and RMG2-HNF1β-sh2, 45.2 ± 8.53%, $P = 0.0047$) relative to the control cells (Figure 3C).

We also analyzed the effect of HNF-1β on glucose metabolism using another OCCC cell line, RMG1. Glucose uptake (69.0 ± 1.60%, $P = 0.0008$; Figure 3D), glycolytic flux (71.5 ± 1.35%, $P = 0.0003$; Figure 3E) and lactic acid production (60.0 ± 0.98%, $P < 0.0001$; Figure 3F) in RMG1-HNF1β-sh1 cells were also significantly suppressed compared to control cells.

Effect of HNF-1β Overexpression on Cell Proliferation, Glucose Uptake, Glycolytic Flux, and Lactate Secretion

Expression of HNF-1β was determined by qRT-PCR and Western blot following transfection of the *HNF-1β* gene construct into Hey ovarian cancer cells. Both the mRNA and protein levels were markedly increased in Hey-HNF1β compared with the Hey-control cells (Figure 2A). Forced expression of HNF-1β in Hey cells led to a decrease in cell proliferation, as measured using the WST-8 assay ($P = 0.0003$; Figure 2B). The PDT of Hey-control and Hey-HNF1β was 11.9 and 14.9 h, respectively.

Glucose uptake was significantly increased in Hey-HNF1β cells when compared with Hey-control cells (231 ± 65.2% vs. 100 ± 28.8%, $P = 0.0334$; Figure 3G). Hey-HNF1β cells also exhibited enhanced glycolytic flux relative to the Hey-control cells (120 ± 7.26% vs. 100 ± 2.84%, $P = 0.0099$; Figure 3H).

Lactate production over the course of 24 h was also elevated in Hey-HNF1β cells compared with that in Hey-control cells (118 ± 7.74% vs. 100 ± 8.37%, $P = 0.0028$; Figure 3I).

Moreover, forced expression of HNF-1β in the immortalized human ovarian surface cell line (HOSE/E7/hTERT) showed a similar result as Hey

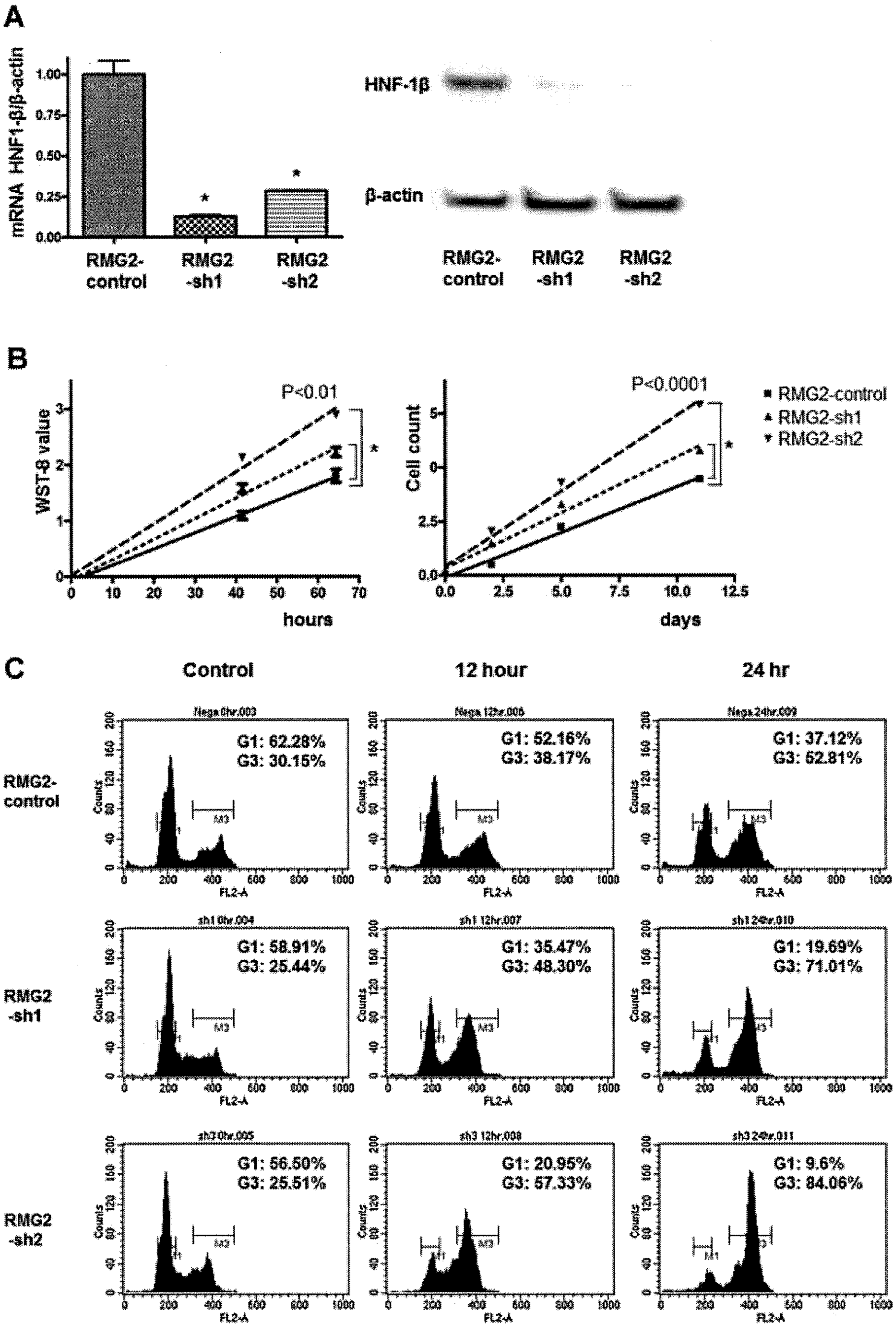

Figure 1. Short hairpin RNA mediated knockdown of HNF-1β expression enhanced cell proliferation rates with suppression of CDKN1A and CDKN1B protein expression and progressed cell cycle the G1/S to G2/M phase. (A) *HNF-1β* mRNA expression detected by quantitative RT-PCR (left panel). HNF-1β protein expression detected by Western blot analysis (right panel). (B) Cell proliferation curve produced from results of the WST-8 assay (left panel). Cell proliferation curve produced by direct cell counts (right panel). *x*-axis, incubation time; *y*-axis, relative number cells in $\log_2$ scale. In detail, relative number cells are determined as WST-8 value (number of cells) divided by WST-8 (number of cells) value at 0 h (0 d). (C) Cell cycle analysis using PI after 12, 24 h nocodazole treatment. (D) The cell cycle analysis using BrdU incorporation. (E) CDKN1B protein expression by Western blot analysis. (F) CDKN1A protein expression by Western blot analysis. The right panels of (E) and (F) showed the quantified protein expressions which were normalized with the expression in control cells. RMG2-sh1, RMG2-HNF1β-sh1; RMG2-sh2, RMG2-HNF1β-sh2; G1, G1 phase; G3, G3 phase; *$P < 0.01$.

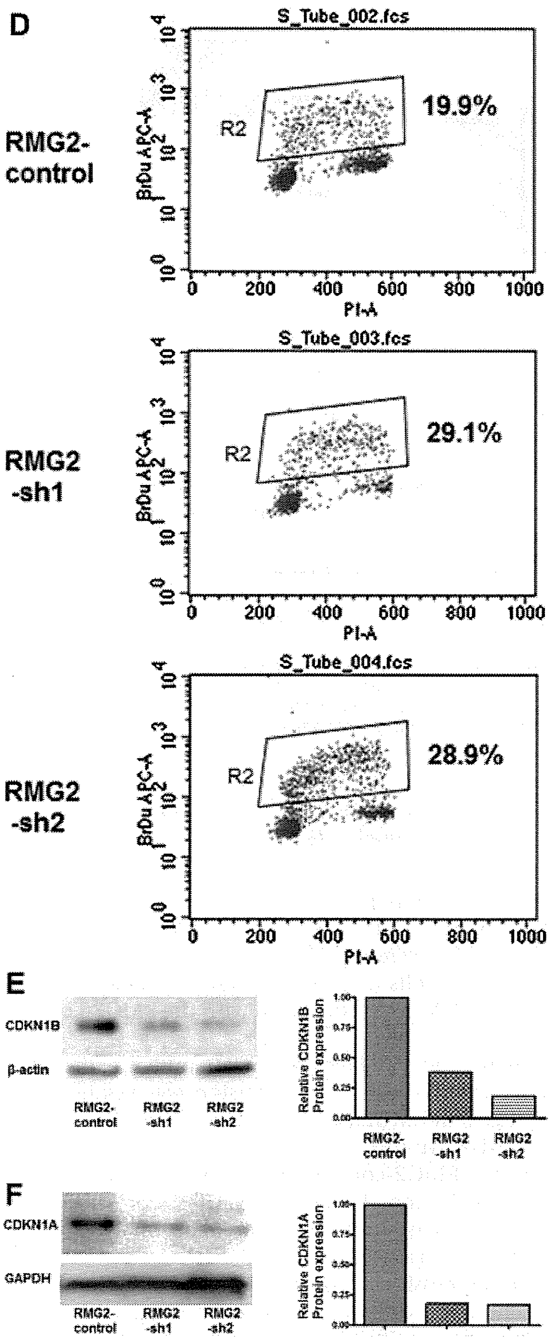

Figure 1. (*Continued*)

cell in glucose uptake, glycolytic flux and lactate production (Supplementary Figure 2).

Effect of HNF-1β Knockdown and Overexpression on GLUT1 Expression

GLUT1 mRNA expression in HNF-1β-knockdown RMG2 cells was evaluated by qRT-PCR and found to be repressed as compared to the control cells (RMG2-HNF1β-sh1, 36.3 ± 0.19%, $P = 0.0001$ and RMG2-HNF1β-sh2, 40.5 ± 0.20%, $P = 0.0001$; Figure 4A). Likewise, the expression of GLUT1 protein was also lower in the HNF-1β-knockdown cells than that observed in the non-silencing control cells (Figure 4B). In addition, the mRNA expression of *GLUT1* in RMG1-HNF1β-sh1 was also decreased as compared to control cells (84.94% ± 1.25%, $P = 0.035$; Figure 4C). GLUT1 protein expression was also suppressed in RMG1-HNF1β-sh1 (Figure 4D).

Inversely, the expression of *GLUT1* mRNA in Hey-HNF1β cells was more than 2-fold higher than that in Hey-control cells (228 ± 11.2% vs. 100 ± 0.98%, $P = 0.0073$; Figure 4E). GLUT1 protein expression was also elevated in the HNF-1β-overexpressing cells (Figure 4F).

Effect of HNF-1β Suppression on Glycolytic Enzymes and HIF-1α Expression

Messenger RNA expression levels of most of the glycolytic enzymes (Hexokinase1 (*HK1*), Hexokinase2 (*HK2*), Glucose-6-phosphate isomerase (*GPI*), Phosphofructokinase liver type (*PFK-L*), Phosphofructokinase platelet type (*PFK-P*), Aldolase A (*ALDOA*), Aldolase B (*ALDOB*), Aldolase C (*ALDOC*), Triosephosphate isomerase (*TPI*), Phosphoglycerate kinase 1 (*PGK1*), Phosphoglycerate kinase 2 (*PGK2*), Phosphoglycerate mutase 1 (*PGAM1*), Enolase 2 (*ENO2*), Enolase 3 (*ENO3*), Lactose dehydrogenase A (*LDHA*), Lactose dehydrogenase B (*LDHB*)) were significantly decreased in RMG2-HNF1β-sh1 cells as compared with the RMG2-control group (Figure 5).

Since HIF-1α is implicated in the stress-resistance in several cell lines, we examined if HNF-1β affects HIF-1α expression. Expression levels of *HIF-1α* mRNA were not significantly different between RMG2-HNF1β-sh1, RMG2-HNF1β-sh2, and RMG2-control cells (Supplementary Figure 3).

Effect of HNF-1β Suppression on OCCC Signature

OCCC signature upregulated genes (393 probe sets) were significantly enriched in the non-silencing control cell group as compared with the HNF-1β-knockdown cells (RMG2-HNF1β-sh1, RMG2-HNF1β-sh2; FDRq-value < 0.0001 and <0.0001, respectively; Figure 6A). OCCC signature downregulated genes (44 probe sets) were significantly enriched in the HNF-1β-knockdown cells when compared with the non-silencing control cells (FDRq-value = 0.0019 and 0.0051, respectively; Figure 6B). These data indicate that by suppressing HNF-1β activity, the OCCC signature profile is altered in a manner that more closely matches the non-OCCC gene signature profile.

Creation of an HNF-1β Signature From HNF-1β-knockdown Microarray Data

We analyzed the gene expression microarray data derived from the HNF-1β-knockdown cells and the

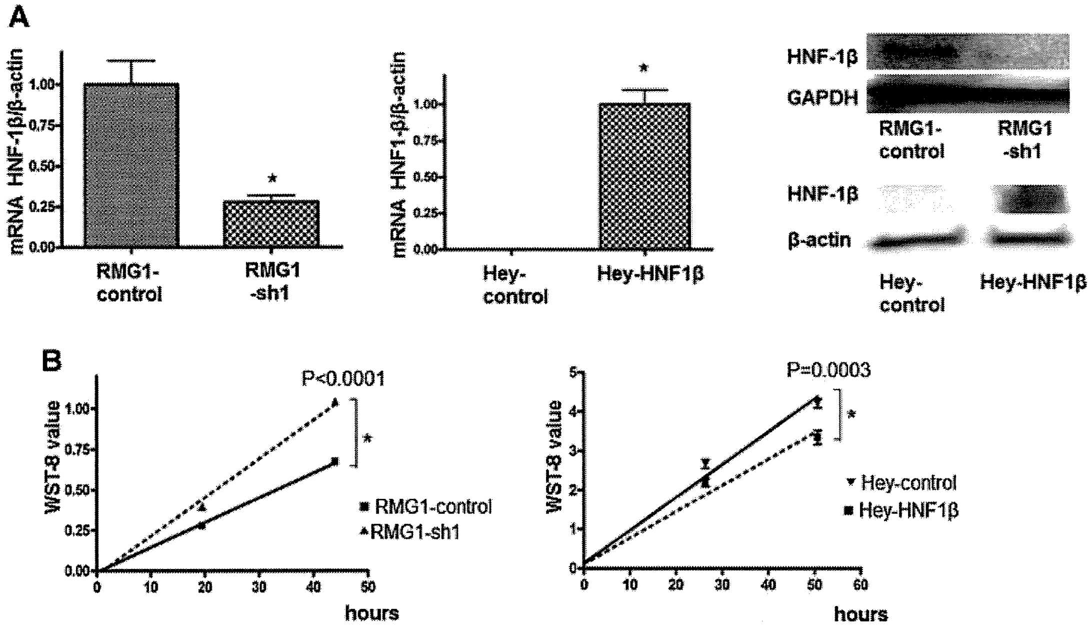

Figure 2. Knockdown of HNF-1β in RMG1 cells and forced expression of HNF-1β in Hey cells also affected the cell proliferation rate. (A) *HNF-1β* mRNA expression detected by quantitative RT-PCR (left and central panel). HNF-1β protein expression by Western blot analysis (right panel). (B) Cell proliferation curve produced from results of the WST-8 assay. RMG1-sh1, RMG1-HNF1β-sh1; $^{*}P<0.05$. Experiments were done three times in triplicate.

non-silencing control cells using Bayesian binary regression 2.0, and derived an HNF-1β signature that consists of 250 probe sets (Supplementary Table 3) that are differentially expressed between these two groups (Figure 6C and D). The HNF-1β signature was able to distinguish OCCC from non-OCCC in the clinical ovarian cancer dataset GSE6008 (HNF-1β signature probability, 0.934 ± 0.0378 in OCCC vs. 0.423 ± 0.208 in non-OCCC, $P<0.0001$) and in dataset GSE2109 (HNF-1β signature probability, 0.632 ± 0.297 in OCCC vs. 0.478 ± 0.224 in non-OCCC, $P=0.0112$), as well as in the ovarian cancer cell line dataset KyotoOv [8] (HNF-1β signature probability, 0.610 ± 0.196 in OCCC vs.0.409 ± 0.221 in non-OCCC, $P=0.012$; Figure 6D).

Effect of GLUT1 Knockdown on Glucose Uptake of RMG2 Cells

Knockdown of GLUT1 was performed using *GLUT1*-specific siRNAs (siRNA1, siRNA2). Over 41.8% (siRNA1) and 49.6% (siRNA2) knockdown of *GLUT1* expression was achieved as measured by qRT-PCR and 87.7% (siRNA1) and 61.7% (siRNA2) reduction in GLUT1 protein levels measured by Western blot (Supplementary Figure 1A and B). Glucose uptake following GLUT1 suppression was decreased relative to that observed in the cells receiving the negative-control siRNA (siRNA1, 73.7 ± 7.72%, $P=0.0074$; siRNA2, 70.8 ± 6.28%, $P=0.0030$; Supplementary Figure 1C).

Effect of HNF-1β Suppression on the Expression of Superoxide Dismutase 1 (*SOD1*)

In the microarray data derived from the HNF-1β-knockdown cells and the non-silencing control cells, the expression of *SOD1*, which is one of oxidative stress genes, were significantly suppressed in RMG2-HNF1β-sh1 cells ($P<0.0001$) and RMG2-HNF1β-sh2 cells ($P=0.0002$) as compared with the RMG2-control (Figure 6F).

Further, we validated the *SOD1* mRNA expression by using qRT-PCR. The expression was significantly decreased in RMG2-HNF1β-sh1 cells ($P=0.0012$) and RMG2-HNF1β-sh2 cells ($P=0.0001$) as compared with the RMG2-control (Figure 6G). Using another OCCC cell line, RMG1, HNF-1β suppression also caused decrease in mRNA expression of *SOD1* genes ($P=0.029$; Figure 6G).

The expression of Glutathione peroxidase (*GPX*), which is also one of the oxidative stress genes, was also decreased in HNF-1β-suppressed cells (Supplementary Figure 4).

DISCUSSION

We previously identified an OCCC-specific gene expression signature that contains multiple genes with functional relevance to the biology of clear cell carcinomas, including *HIF-1α*, *IL-6*, and *HNF-1β*. In this study, we focused on the role of HNF-1β in OCCC for several reasons. First, HNF-1β is overexpressed

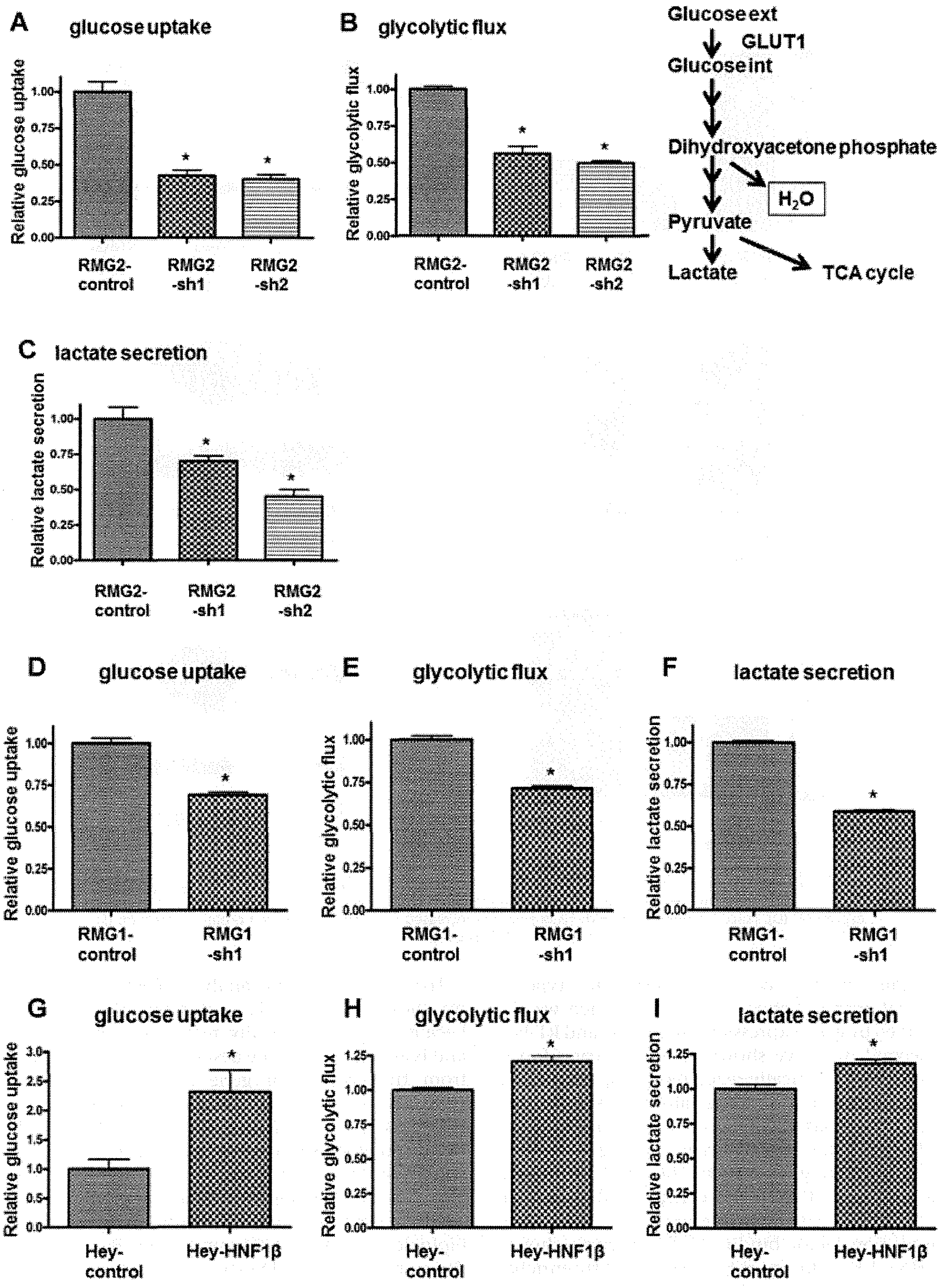

Figure 3. Knockdown of HNF-1β in RMG2 and RMG1 cells was associated with the decrease of glucose uptake, glycolytic flux, and lactate secretion. Conversely, forced expression of HNF-1β in Hey cells was associated with the increase of them. (A) Glucose uptake in RMG2 cells. (B) Glycolytic flux in RMG2 cells (left panel). Scheme of simplified glycolytic pathway (right panel). (C) Lactate secretion in RMG2 cells. (D) Glucose uptake in RMG1 cells. (E) Glycolytic flux in RMG1 cells. (F) Lactate secretion in RMG1 cells. (G) Glucose uptake in Hey cells. (H) Glycolytic flux in Hey cells. (I) Lactate secretion in Hey cells. RMG2-sh1, RMG2-HNF1β-sh1; RMG2-sh2, RMG2-HNF1β-sh2; RMG1-sh1, RMG1-HNF1β-sh1. $^*P < 0.05$.

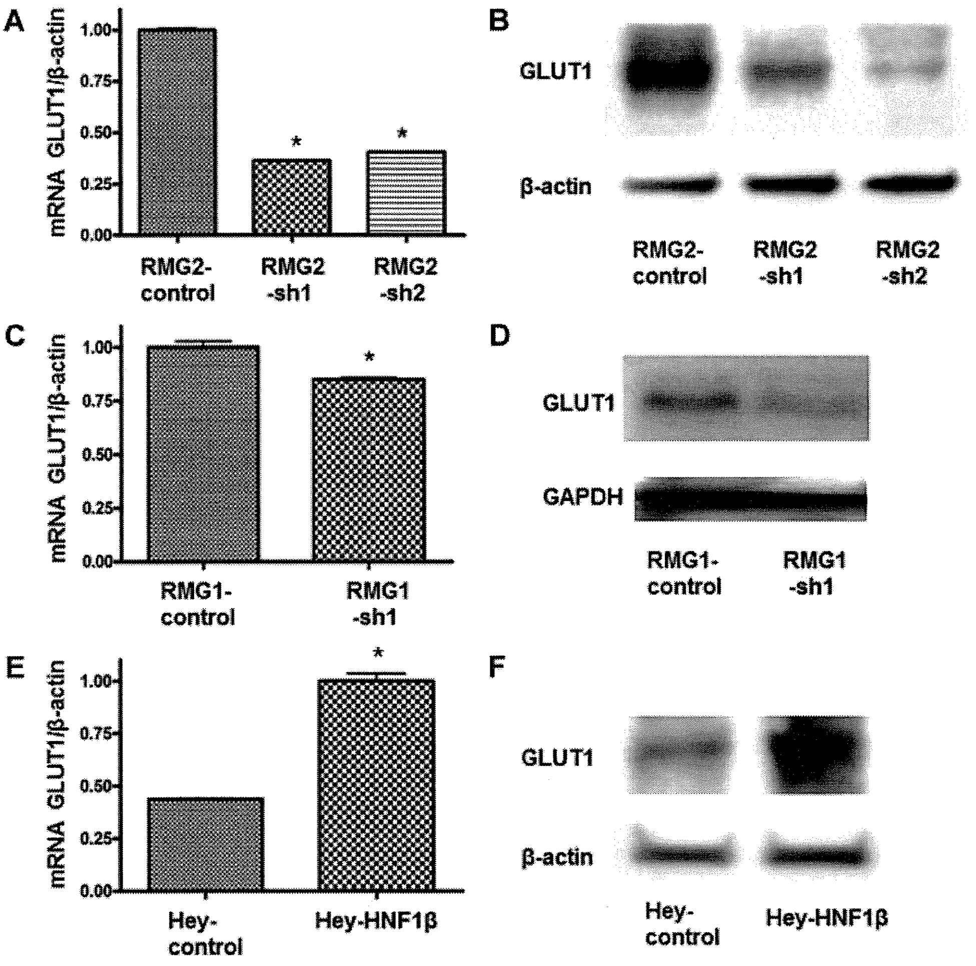

Figure 4. HNF-1β upregulated GLUT1 expression. Knockdown of HNF-1β expression in RMG2 suppressed *GLUT1* mRNA (A) and protein (B). Knockdown of HNF-1β expression in RMG1 suppressed *GLUT1* mRNA (C) and protein expression (D). Forced expression of HNF-1β in Hey cells increased *GLUT1* mRNA (E) and protein expression (F). RMG2-sh1, RMG2-HNF1β-sh1; RMG2-sh2, RMG2-HNF1β-sh2; RMG1-sh1, RMG1-HNF1β-sh1. $^*P < 0.05$.

specifically in the clear cell histologic type of epithelial ovarian cancer [12,17–19], which we also confirmed by gene expression microarray and RT-PCR [8]. Second, we have shown that the expression of HNF-1β is epigenetically regulated [8,20], which is an important and pharmacologically reversible feature of many cancer-associated genes. Third, activation of the HNF-1β signaling network was strongly predicted from the pathway analysis of the OCCC signature, indicating that HNF-1β is a central mediator of the OCCC-specific signaling network [8,13]. Finally, transcription factor binding motif analysis showed that HNF-1β binding motifs are significantly enriched among genes that comprise the OCCC signature [13]. Taken together, these findings strongly suggested that HNF-1β plays a central role in the manifestation of the unique biological phenotype of OCCC, but the mechanisms driving this have been thus far unclear.

To begin a functional analysis of HNF-1β in OCCC, we chose to use RMG2, a human OCCC cell line, because it phenotypically resembles clinical OCCC and is also thought to be best representative of OCCC from the context of gene expression profiles as measured by microarray analyses. Knockdown of HNF-1β expression in RMG2 cells using lentiviral transfer of gene-specific shRNAs resulted in a marked shift in the OCCC signature toward a non-OCCC gene expression profile, suggesting that, as predicted, HNF-1β is a key molecule in maintaining an OCCC biological phenotype (Figure 6A and B). To confirm the significance of HNF-1β in OCCC, we also used binary regression 2.0 to develop an HNF-1β gene signature using gene expression microarray data obtained from HNF-1β-knockdown and control cells. The HNF-1β gene signature consists of the group of genes that are differentially expressed between the HNF-1β-knockdown and control RMG2 cells, and has

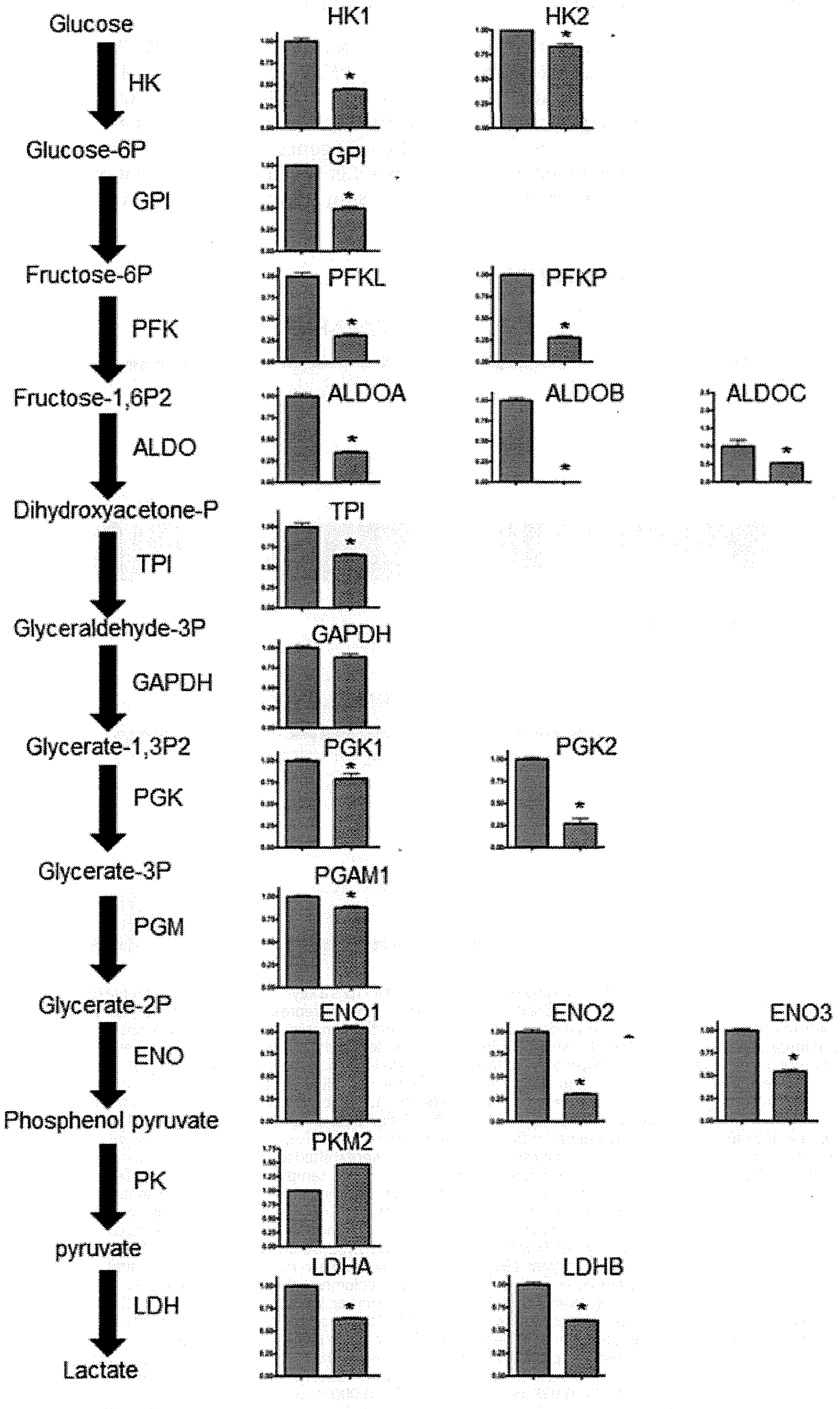

Figure 5. Effect of HNF-1β suppression on glycolytic enzymes Messenger RNA expression of *HK1*, *HK2*, *GPI*, *PFK-L*, *PFK-P*, *ALD-A*, *ALD-B*, *ALDOC*, *TPI*, *PGK1*, *PGK2*, *PGAM 1*, *ENO2*, *ENO3*, *LDHA*, and *LDHB* were decreased in RMG2-HNF1β-sh1 (right bar) cells, relative to RMG2-control cells (left bar). *HK*, hexokinase; *GPI*, glucose-6-phosphate isomerase; *PFK-L*, phosphofructokinase liver type; *PFK-P*, phosphofructokinase platelet type; *ALD*, aldolase; *TPI*, triosephosphate isomerase; *GAPDH*, glyceraldehyde-3-phosphate dehydrogenase; *PGK*, phosphoglycerate kinase; *PGAM*, phosphoglycerate mutase; *ENO*, enolase; *PKM*, pyruvate kinase muscle type; *LDH*, lactate dehydrogenase. $^*P < 0.05$. Experiments were done in duplicate.

the ability to distinguish OCCC from non-OCCC in both ovarian cancer cell line datasets and importantly, clinical ovarian cancer datasets (Figure 6C–E). These results support that HNF-1β plays a pivotal role in the biology of OCCC. In addition, a total of 23 genes including HNF-1β were overlapped between OCCC- and HNF-1β signature. Among them, eight genes (*ELOVL6, FXYD2, IVNS1ABP, LIPC, MED28, MITF, RELN, TNFAIP6*) have HNF-1 binding element (V$HNF1 01) by analyzing with GATHER software (http://gather.genome.duke.edu/). We also analyzed these 23 genes by DAVID software (http://david.abcc.ncifcrf.gov/), and found that genes belonging to GO slim terms related to cell proliferation and

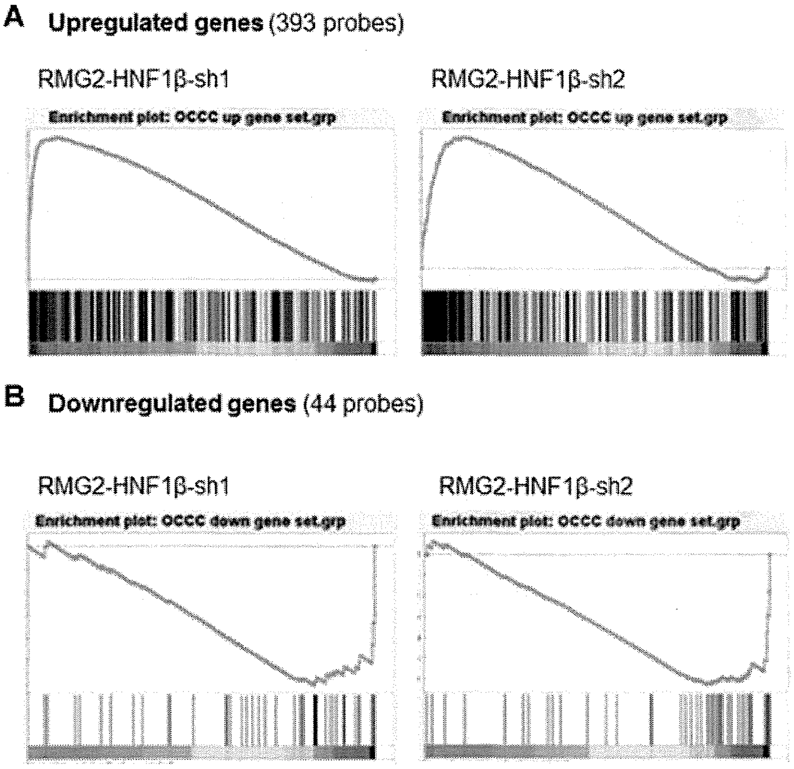

Figure 6. Gene expression microarray analysis showed that HNF-1β is a key molecule determining the OCCC gene expression profile. (A and B) Gene Set Enrichment Analysis. The *x*-axis represents rank of genes comprising of a particular gene set (signature genes) among the whole genes in the genome. Each vertical black line represents on signature genes, and the degree to which the black lines are deviated to the left or right indicates the statistical significance regarding increased expression of the signature genes in a particular group of samples (designated as enrichment). The *y*-axis represents Enrichment Score (ES) of the individual signature genes. Shift of the green line curve to the upper left indicates enrichment in the left, and shift to the lower right indicates enrichment in the right. (A) Left *x*-axis; Individual upregulated genes within the OCCC signature are shown as vertical black lines to see their deviation compared to the whole genes in the genome between the left (control shRNA samples, $n = 10$) and the right (HNF1β-sh1, $n = 5$). The genes comprising of this gene set were shifted to the left, which indicates enrichment in the RMG2-control-sh samples as compared to RMG2-HNF1β-sh1 samples (FDRq-value < 0.0001). (A) Right; Similarly, the upregulated genes within the OCCC signature were enriched in the RMG2-control-sh samples ($n = 10$) as compared to the RMG2-HNF1β-sh2 samples ($n = 5$) (FDRq-value < 0.0001). (B) The downregulated genes within the OCCC signature were significantly enriched in RMG2-HNF1β-sh1 and RMG2-HNF1β-sh2 cells as compared with RMG2-control cells (FDRq-value = 0.0019 and 0.0051, respectively). (C) Analysis using Bayesian binary regression. The HNF-1β signature was generated from 250 probe sets shown in each row. Red to blue indicates high to low expression. Each column represents an individual cell line. Ten columns on the left side represent shRNAs (both RMG2-HNF1β-sh1 and RMG2-HNF1β-sh2 cells) and the ten columns on the right side represent RMG2-control cells. (D) Leave-one-out cross-validation of training sets (RMG2-HNF1β-sh1 and RMG2-HNF1β-sh2 cells versus RMG2-control) using the HNF-1β signature genes. Blue and red colors indicate RMG2-HNF1β-sh cells ($n = 10$) and RMG2-control cells ($n = 10$), respectively. The probability estimates based on the HNF-1β signature genes is shown on the vertical axis with 95% confidence intervals. (E) OCCC has a higher probability of having the HNF-1β signature profile than non-OCCC. GSE6008 (0.93 ± 0.038 vs. 0.42 ± 0.21, $P < 0.0001$); GSE2109 (0.63 ± 0.30 vs. 0.48 ± 0.22, $P = 0.0112$); KyotoOv (0.61 ± 0.20 vs. 0.41 ± 0.22, $P = 0.012$). (F) The expression of *SOD1* gene (probe ID: 200642_at) is significantly decreased in RMG2-HNF1β-sh1 and RMG2-HNF1β-sh2 cells as compared to control cells ($P < 0.0001$ and $P = 0.0002$, respectively). (G) The validation of *SOD1* gene expression by qRT-PCR. RMG2-HNF1β-sh1 and RMG2-HNF1β-sh2 cells versus RMG2-control cells ($P = 0.0012$ and $P = 0.0001$, respectively). RMG1-HNF1β-sh1 versus RMG1-control cells ($P = 0.029$). RMG2-sh1, RMG2-HNF1β-sh1; RMG2-sh2, RMG2-HNF1β-sh2; RMG1-sh1, RMG1-HNF1β-sh1. $^*P < 0.05$.

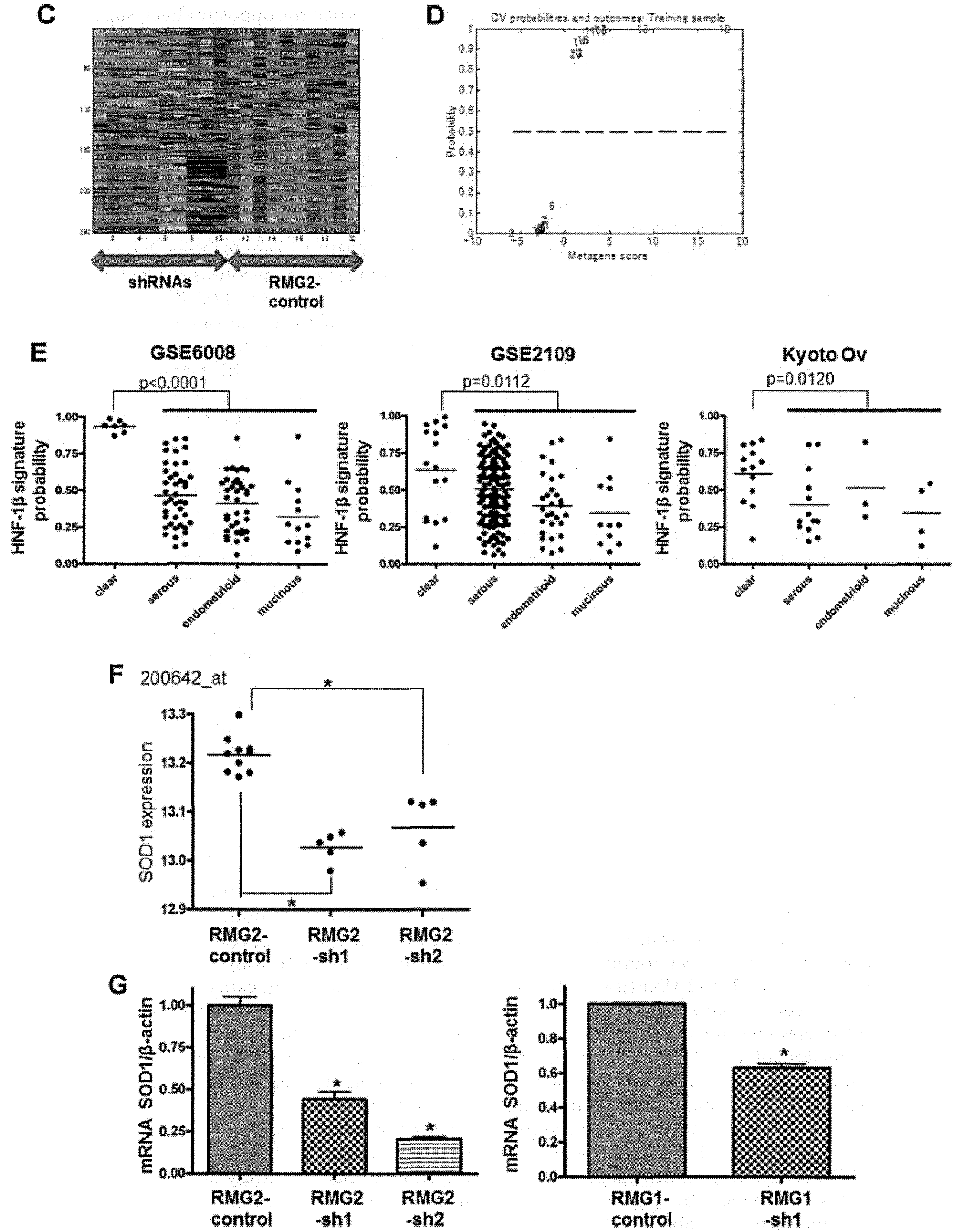

Figure 6. (*Continued*)

metabolism such as "negative regulation of cell proliferation ($P = 0.09$)," "carbohydrate binding ($P = 0.062$)," and "regulation of cellar response to stress ($P = 0.009$)" were enriched in these 23 genes.

Then, we tested if HNF-1β suppression affects cell proliferation and notably found that this significantly increases the growth rate of RMG2 cells. Moreover, transfection of the *HNF-1β* gene into Hey, a serous ovarian cancer cell line with minimal HNF-1β expression, caused cell growth to be significantly decreased. These data suggest that HNF-1β functions as a suppressive regulator of cell proliferation. We then evaluated whether HNF-1β suppression causes leads to altered expression of the cell cycle regulator, CDKN1A and CDKN1B, and found that it causes marked reduction of CDKN1A and CDKN1B levels, suggesting that HNF-1β negatively controls cell proliferation by inducing expression of a potent cell cycle regulatory gene that inhibits G1 progression. As shown in Supplementary Table 4, *CDKN1B* has HNF-1 binding motif according to TRANSFAC dataset [21]. The cell cycle analysis using flow cytometry also suggests that HNF-1β act as inhibitor of cell cycle progression. Suppression of HNF-1β significantly increased cell population in S-phase. Taken together, observation of clinical cases as well as ovarian cancer cell lines indicates that OCCC generally grows slower than serous adenocarcinoma, which may partly be ascribed to the overexpression of HNF-1β in OCCC [3].

It is well documented that cancer cells exhibit unusually active metabolic processes when compared with normal cells. This "metabolic switch" in cancer cells is most prominent with regard to glucose metabolism [22–24]. In this study, we incidentally noticed that the culture media over time retained its red coloration from the phenol red (which is indicative of a more basic pH levels) in spite of the increased growth rate of the HNF-1β-knockdown RMG2 cells, suggesting that these cells may be secreting less lactate into the media. Indeed, measurement of lactate indicated that both RMG2-HNF1β-sh1 and RMG2-HNF1β-sh2 show significantly less efflux of lactate when compared with the RMG2-control. We then evaluated glucose uptake in these cells and found that it is also significantly lower in RMG2-HNF1β-sh1 and RMG2-HNF1β-sh2 cells than in the RMG2-control cells. Expression of the glucose transporter *GLUT1* mRNA as well as GLUT1 protein was found to be lower in RMG2-HNF1β-sh1 and RMG2-HNF1β-sh2 than in the RMG2-control cells. Conversely, forced expression of HNF-1β in Hey cells increased glucose uptake as well as expression of GLUT1. Furthermore, the observed significant reduction in glucose uptake in RMG2 cells following GLUT1 knockdown confirmed a major role of GLUT1 in mediating glucose transport in these cells (Supplementary Figure 1). In addition, *GLUT1* had HNF-1 binding motif according to TRANSFAC dataset provided by Jeffrey T. et al. (2006) [21] (Supplementary Table 4). These data suggest that HNF-1β increases glucose uptake at least in part by upregulating a glucose transporter gene.

We further evaluated the role of HNF-1β in glucose metabolism using an assay that measures glycolytic flux within cells. Knockdown of HNF-1β in RMG2 cells decreased the glycolytic flux rate in comparison with the control cells, while forced expression of HNF-1β in Hey cells had the opposite effect, suggesting that HNF-1β not only increases glucose uptake but also promotes glycolysis in cancer cells. In fact, further evaluation of gene expression related to the enzymatic activity associated with the glycolytic process revealed that a majority of the genes examined were repressed by HNF-1β knockdown. As shown in Supplementary Table 4, some of these glycolytic enzymes have HNF-1 binding motif according to TRANSFAC dataset [21]. It has been reported that activation of HIF-1α causes upregulation of GLUT1, glucose uptake, and glycolysis under hypoxic conditions [25–27]. Stany et al. [28] also showed that HIF-α pathway was activated as one of specific signaling pathways related to glucose metabolism in OCCC compared with those in high-grade serous ovarian cancer. HIF-1α protein is regulated at the posttranslational level via the ubiquitin-proteasome system under normoxic condition. In this study, we found that HNF-1β did not alter either mRNA or protein expressions of HIF-1α (Supplementary Figure 3). Therefore, HNF-1β is not likely to affect transcriptional or posttranscriptional levels of HIF-1α protein. On the other hand, HIF-2α is highly homologous and has similar binding motif as HIF-1α [29]. Therefore, we cannot exclude the possibility that HNF-1β might regulate the glycolytic pathway through HIF-2α.

The characteristically high glycolytic rate in cancer cells was first described by Otto Warburg and is referred to as the "Warburg effect" [30]. According to Warburg's observations, unlike normal tissue cells, cancer cells use glycolysis instead of using mitochondrial oxidative phosphorylation to obtain ATP, which leads to high glucose consumption and lactate production. Although not completely understood, it is presumed that this mechanism is used to meet the metabolic requirements to support rapid proliferation of cancer cells. Indeed, a similar metabolic switch is sometimes observed in normal physiological processes, such as embryonic development, wound healing, or immune reactions during which rapid cell proliferation is required [22]. In cancer cells, some oncogenic alterations have been shown to evoke the Warburg effect [31–34]. In this study, for the first time, we demonstrated that an important function of HNF-1β is to promote the glycolytic process, namely the Warburg effect.

The reason why HNF-1β functions in this manner in OCCC is yet to be elucidated. However, it is noteworthy that this study also found that HNF-1β suppresses cell proliferation along with promoting glycolysis. Hence, increased glycolytic metabolism does not occur in parallel to increased cell proliferation with regard to HNF-1β function, similar to the case of many oncogenes [35]. These findings may indicate that the reasons for overexpression of HNF-1β in OCCC may not necessarily be to meet energy requirements for cell proliferation. Inversely, serous ovarian cancer, typically more rapidly growing tumors than OCCC, seldom show HNF-1β overexpression. Recently, elevated glycolytic rates have been shown to contribute to the inhibition of oxidative stress-induced apoptosis in cancer cells as well as in normal cells, under some conditions [36,37]. We have shown that OCCC arises in the extraordinarily stressful environment of oxygen free radical-enriched endometriotic cysts and expresses significantly more stress-related genes as compared to other histologic types of epithelial ovarian cancers [8]. In this context, HNF-1β may act as a stress-reducer that allows for survival of OCCC cells, although further study is needed to test this hypothesis.

ACKNOWLEDGMENTS

The experiments using radioisotope were performed in the Radioisotope Research Center of Kyoto University and Timothy Haystead's Laboratory of Duke University with helpful assistance from the staff. We also gratefully acknowledge the excellent technical assistance of Yuko Hosoe and Maki Kurokawa.

REFERENCES

1. Mandai M, Yamaguchi K, Matsumura N, Baba T, Konishi I. Ovarian cancer in endometriosis: Molecular biology, pathology, and clinical management. Int J Clin Oncol 2009;14:383–391.
2. Kobayashi H. Ovarian cancer in endometriosis: Epidemiology, natural history, and clinical diagnosis. Int J Clin Oncol 2009;14:378–382.
3. Itamochi H, Kigawa J, Terakawa N. Mechanisms of chemoresistance and poor prognosis in ovarian clear cell carcinoma. Cancer Sci 2008;99:653–658.
4. Kobayashi H, Sumimoto K, Moniwa N, et al. Risk of developing ovarian cancer among women with ovarian endometrioma: A cohort study in Shizuoka, Japan. Int J Gynecol Cancer 2007;17:37–43.
5. Sugiyama T, Kamura T, Kigawa J, et al. Clinical characteristics of clear cell carcinoma of the ovary: A distinct histologic type with poor prognosis and resistance to platinum-based chemotherapy. Cancer 2000;88:2584–2589.
6. Goff BA, Sainz de la Cuesta R, Muntz HG, et al. Clear cell carcinoma of the ovary: A distinct histologic type with poor prognosis and resistance to platinum-based chemotherapy in stage III disease. Gynecol Oncol 1996;60:412–417.
7. Yamaguchi K, Mandai M, Toyokuni S, et al. Contents of endometriotic cysts, especially the high concentration of free iron, are a possible cause of carcinogenesis in the cysts through the iron-induced persistent oxidative stress. Clin Cancer Res 2008;14:32–40.
8. Yamaguchi K, Mandai M, Oura T, et al. Identification of an ovarian clear cell carcinoma gene signature that reflects inherent disease biology and the carcinogenic processes. Oncogene 2010;29:1741–1752.
9. Bach I, Mattei MG, Cereghini S, Yaniv M. Two members of an HNF1 homeoprotein family are expressed in human liver. Nucleic Acids Res 1991;19:3553–3559.
10. Bingham C, Hattersley AT. Renal cysts and diabetes syndrome resulting from mutations in hepatocyte nuclear factor-1beta. Nephrol Dial Transplant 2004;19:2703–2708.
11. Maestro MA, Cardalda C, Boj SF, Luco RF, Servitja JM, Ferrer J. Distinct roles of HNF1beta, HNF1alpha, and HNF4alpha in regulating pancreas development, beta-cell function and growth. Endocr Dev 2007;12:33–45.
12. Tsuchiya A, Sakamoto M, Yasuda J, et al. Expression profiling in ovarian clear cell carcinoma: Identification of hepatocyte nuclear factor-1 beta as a molecular marker and a possible molecular target for therapy of ovarian clear cell carcinoma. Am J Pathol 2003;163:2503–2512.
13. Matsumura N, Mandai M, Okamoto T, et al. Sorafenib efficacy in ovarian clear cell carcinoma revealed by transcriptome profiling. Cancer Sci 2010;101:2658–2663.
14. Wakasugi M, Matsuura K, Nagasawa A, et al. DDB1 gene disruption causes a severe growth defect and apoptosis in chicken DT40 cells. Biochem Biophys Res Commun 2007; 364:771–777.
15. Shi DY, Xie FZ, Zhai C, Stern JS, Liu Y, Liu SL. The role of cellular oxidative stress in regulating glycolysis energy metabolism in hepatoma cells. Mol Cancer 2009;8:32.
16. Kondoh H, Lleonart ME, Gil J, et al. Glycolytic enzymes can modulate cellular life span. Cancer Res 2005;65:177–185.
17. Kato N, Toukairin M, Asanuma I, Motoyama T. Immunocytochemistry for hepatocyte nuclear factor-1beta (HNF-1beta): A marker for ovarian clear cell carcinoma. Diagn Cytopathol 2007;35:193–197.
18. Kao YC, Lin MC, Lin WC, Jeng YM, Mao TL. Utility of hepatocyte nuclear factor-1beta as a diagnostic marker in ovarian carcinomas with clear cells. Histopathology 2012;61:760–768.
19. Fadare O, Liang SX. Diagnostic utility of hepatocyte nuclear factor 1-beta immunoreactivity in endometrial carcinomas: Lack of specificity for endometrial clear cell carcinoma. Appl Immunohistochem Mol Morphol 2012;20:580–587.
20. Kato N, Tamura G, Motoyama T. Hypomethylation of hepatocyte nuclear factor-1beta (HNF-1beta) CpG island in clear cell carcinoma of the ovary. Virchows Arch 2008;452:175–180.
21. Chang JT, Nevins JR. GATHER: A systems approach to interpreting genomic signatures. Bioinformatics 2006;22:2926–2933.
22. Levine AJ, Puzio-Kuter AM. The control of the metabolic switch in cancers by oncogenes and tumor suppressor genes. Science 2010;330:1340–1344.
23. Mentis AF, Kararizou E. Metabolism and cancer: An up-to-date review of a mutual connection. Asian Pac J Cancer Prev 2010; 11:1437–1444.
24. DeBerardinis RJ. Is cancer a disease of abnormal cellular metabolism? New angles on an old idea. Genet Med 2008;10:767–777.
25. Marin-Hernandez A, Gallardo-Perez JC, Ralph SJ, Rodriguez-Enriquez S, Moreno-Sanchez R. HIF-1alpha modulates energy metabolism in cancer cells by inducing over-expression of specific glycolytic isoforms. Mini Rev Med Chem 2009;9:1084–1101.
26. Gillies RJ, Gatenby RA. Adaptive landscapes and emergent phenotypes: Why do cancers have high glycolysis? J Bioenerg Biomembr 2007;39:251–257.
27. Semenza GL. HIF-1 mediates the Warburg effect in clear cell renal carcinoma. J Bioenerg Biomembr 2007;39:231–234.
28. Stany MP, Vathipadiekal V, Ozbun L, et al. Identification of novel therapeutic targets in microdissected clear cell ovarian cancers. PLoS ONE 2011;6:e21121.25.
29. Li Z, Bao S, Wu Q, et al. Hypoxia-inducible factors regulate tumorigenic capacity of glioma stem cells. Cancer Cell 2009; 15:501–513.
30. Warburg O. On the origin of cancer cells. Science 1956;123:309–314.
31. Maddocks OD, Vousden KH. Metabolic regulation by p53. J M l Med 2011;89:237–245.
32. Kondoh H. Cellular life span and the Warburg effect. Exp Cell Res 2008;314:1923–1928.
33. Dang CV, Le A, Gao P. MYC-induced cancer cell energy metabolism and therapeutic opportunities. Clin Cancer Res 2009;15:6479–6483.

34. Yeung SJ, Pan J, Lee MH. Roles of p53, MYC and HIF-1 in regulating glycolysis—The seventh hallmark of cancer. Cell Mol Life Sci 2008;65:3981–3999.
35. Fritz V, Fajas L. Metabolism and proliferation share common regulatory pathways in cancer cells. Oncogene 2010;29: 4369–4377.
36. Kondoh H, Lleonart ME, Bernard D, Gil J. Protection from oxidative stress by enhanced glycolysis; a possible mechanism of cellular immortalization. Histol Histopathol 2007;22: 85–90.
37. Ruckenstuhl C, Buttner S, Carmona-Gutierrez D, et al. The Warburg effect suppresses oxidative stress induced apoptosis in a yeast model for cancer. PLoS ONE 2009;4:e4592.

SUPPORTING INFORMATION

Additional supporting information may be found in the online version of this article at the publisher's web-site.

TRANSPARENT PROCESS
OPEN ACCESS
EMBO Molecular Medicine

Functional genomics identifies five distinct molecular subtypes with clinical relevance and pathways for growth control in epithelial ovarian cancer

Tuan Zea Tan[1†], Qing Hao Miow[1,2†], Ruby Yun-Ju Huang[1,3†], Meng Kang Wong[1], Jieru Ye[1], Jieying Amelia Lau[1], Meng Chu Wu[1], Luqman Hakim Bin Abdul Hadi[1], Richie Soong[1], Mahesh Choolani[3], Ben Davidson[4,5], Jahn M. Nesland[4,5], Ling-Zhi Wang[1,6], Noriomi Matsumura[7], Masaki Mandai[7], Ikuo Konishi[7], Boon-Cher Goh[1,6,8], Jeffrey T. Chang[9], Jean Paul Thiery[1,10,11], Seiichi Mori[1,11,12]**,‡*

Keywords: cell line model for subtype; functional genomic screen; molecular subtype; ovarian cancer; tubulin

DOI 10.1002/emmm.201201823

Received August 06, 2012
Revised April 03, 2013
Accepted April 09, 2013

Epithelial ovarian cancer (EOC) is hallmarked by a high degree of heterogeneity. To address this heterogeneity, a classification scheme was developed based on gene expression patterns of 1538 tumours. Five, biologically distinct subgroups — Epi-A, Epi-B, Mes, Stem-A and Stem-B — exhibited significantly distinct clinicopathological characteristics, deregulated pathways and patient prognoses, and were validated using independent datasets. To identify subtype-specific molecular targets, ovarian cancer cell lines representing these molecular subtypes were screened against a genome-wide shRNA library. Focusing on the poor-prognosis Stem-A subtype, we found that two genes involved in tubulin processing, *TUBGCP4* and *NAT10*, were essential for cell growth, an observation supported by a pathway analysis that also predicted involvement of microtubule-related processes. Furthermore, we observed that Stem-A cell lines were indeed more sensitive to inhibitors of tubulin polymerization, vincristine and vinorelbine, than the other subtypes. This subtyping offers new insights into the development of novel diagnostic and personalized treatment for EOC patients.

---

(1) Cancer Science Institute of Singapore, National University of Singapore, Singapore
(2) NUS Graduate School for Integrative Sciences and Engineering, National University of Singapore, Singapore
(3) Department of Obstetrics and Gynecology, National University Health System, Singapore
(4) Division of Pathology, Norwegian Radium Hospital Oslo University Hospital, Oslo, Norway
(5) Faculty of Medicine, University of Oslo, Institute of Clinical Medicine, Oslo, Norway
(6) Department of Pharmacology, National University of Singapore, Singapore
(7) Department of Obstetrics and Gynecology, Kyoto University, Kyoto, Japan
(8) Department of Hematology and Oncology, National University Health System, Singapore
(9) Department of Integrative Biology and Pharmacology, University of Texas Health Science Center at Houston, TX, USA
(10) Institute of Molecular and Cell Biology, A*STAR (Agency for Science, Technology and Research), Singapore
(11) Department of Biochemistry, National University of Singapore, Singapore
(12) Division of Cancer Genomics, Cancer Institute of Japanese Foundation for Cancer Research, 3-8-31 Ariake, Koto-ku, Tokyo, Japan
***Corresponding author:** Tel: +65 6516 3241/42; +65 91472036; Fax: +65 6779 1453; E-mail: jpthiery@imcb.a-star.edu.sg
****Corresponding author:** Tel: +81 3 3570 0450; Fax: +81 3 3570 0454; E-mail: seiichi.mori@jfcr.or.jp

[†] These authors contributing equally to this work.
[‡] Present Address: Division of Cancer Genomics, Cancer Institute of Japanese Foundation for Cancer Research, Koto-ku, Tokyo, Japan

INTRODUCTION

Epithelial ovarian cancer (EOC) is the most lethal gynaecologic malignancy. The global disease burden is approximately 225,000 new cases per year with a survival rate of 30% (Bray et al, 2013). EOC, like most other cancers, represents a heterogeneous collection of distinct diseases that arise as a consequence of varied somatic mutations and epigenetic changes acquired during the process of tumourigenesis and tumour progression. This heterogeneity is apparent in tumour histopathology such as serous, mucinous, endometrioid and clear cell histotypes. It is now established that the discrete histological types differ with respect to variable clinical features, including epidemiological risk, spread patterns, somatic mutations, chemotherapeutic response and patient prognosis (Gilks & Prat, 2009). The histologically distinct subtype, high-grade serous adenocarcinoma, is the most common subtype and accounts for approximately 70% of all ovarian carcinoma. Although this histotype has distinguishing clinical characteristics from the other subtypes, patients with this histological subtype still show diverse outcomes and usually low survival rates, even after the same or very similar treatment regimens (Gilks & Prat, 2009). One possible reason for this low survival rate is that the high degree of heterogeneity of EOC is not considered in the current standard of care (Vaughan et al, 2011). Thus, it is critically important to develop a systematic scheme to dissect the heterogeneity of EOC (Bast et al, 2009; Vaughan et al, 2011).

Genome-scale expression data has been instrumental in characterizing the complex biological diversity of human cancer (Alizadeh et al, 2000; Perou et al, 2000; Verhaak et al, 2010). Subtypes identified through expression microarray analyses are coupled with multiple clinical parameters, such as patient prognosis, age of onset and molecular marker expression (Alizadeh et al, 2000; Perou et al, 2000; Verhaak et al, 2010). Efforts to dissect EOC heterogeneity have correlated expression patterns with clinical features, such as histological types, aggressiveness and patient outcomes (Denkert et al, 2009; Helland et al, 2011; Mok et al, 2009; The Cancer Genome Atlas Research Network, 2011; Tothill et al, 2008). However, due to varied sample sizes and analytical criteria, the reported subtypes of EOC are similar but not completely the same (Helland et al, 2011; The Cancer Genome Atlas Research Network, 2011; Tothill et al, 2008; Verhaak et al, 2013), with reports of six molecular subtypes in 285 serous and endometrioid EOC (Tothill et al, 2008), yet only four molecular subtypes in 489 high-grade serous EOC (The Cancer Genome Atlas Research Network, 2011). Thus, a refined classification scheme with intense phenotypic characterization remains to be established. Also, the molecular targets relevant to cancer cell growth in these transcriptional subtypes have not been identified. The development of diagnostic and therapeutic strategies based on such a scheme is paramount for improving therapeutic efficacy in patients with EOC.

Despite recent successes with molecular targeted therapies for chronic myelogenous leukaemia, ER- or Her2-positive breast cancer, and EGFR-mutated lung cancer, targeted therapies for EOC have not been as encouraging (Quintas-Cardama et al, 2009; Rosell et al, 2010; Yaziji et al, 2004). One approach for the identification of specific targets for EOC subtypes is the use of a genome-wide, systematic, functional assessment of cancer cell growth (proliferation and/or viability). The recent success in suppressing the growth of cultured lung cancer cells with activating *EGFR* mutations by siRNA (Sordella et al, 2004) unveiled the sensitivity of siRNA-based approaches in distinguishing drivers of tumour growth. RNAi libraries, such as The RNAi Consortium (TRC) lentiviral library (Moffat et al, 2006; Root et al, 2006), have enabled systematic genetic studies in mammalian cells, and have identified the genes responsible for proliferation and viability in human cancer cell lines, particularly in the context of synthetic lethality (Barbie et al, 2009; Luo et al, 2008; Scholl et al, 2009).

The TRC library contains 80,000 lentivirally expressing short hairpin RNAs (shRNAs), corresponding to 16,000 human genes. In a systematic screen, a library such as this could be employed to help isolate key regulators of cancer cell growth on a genome-wide scale in a pooled format. Cultured cells would be infected with a pool of the shRNA-expressing lentivirus library such that a typical cell is subjected to only one integration event of an shRNA-expressing lentiviral genome into the host. Infected cells would then be allowed to proliferate for a period of time to permit the amplification or depletion of hairpins accordingly. Although the vast majority of shRNAs have minimal effects on cell proliferation and/or viability, an shRNA that silences the expression of a critical gene will be relatively depleted. Conversely, the relative amplification of an shRNA suggests that it targets a gene with an inhibitory role in cell growth. These integrated hairpins are then subsequently retrieved from the genomic DNA by PCR amplification, and the abundance of each shRNA sequence can be measured with microarray hybridization (Luo et al, 2008) or with next-generation sequencing technology (Sims et al, 2011).

Notably, the successful application of this platform led to the discovery of *PAX8* as having a more essential role in proliferation and survival in ovarian cancer cell lines than in cell lines from other tissues (Cheung et al, 2011). Furthermore, *TBK1* was identified as a synthetic lethal partner of oncogenic *KRAS* in an earlier report using this method (Barbie et al, 2009). Despite these successes, this technology has not been used to identify subtype-specific growth-promoting genes, particularly in the context of ovarian cancer.

Here, we describe a functional genomic approach to dissect the heterogeneity of EOC. We established a large-scale meta-analysis of EOC microarray datasets to determine EOC molecular subtypes. Next, we integrated EOC cell line data into the molecular subtyping scheme to derive an *in vitro* working model representative of each molecular subtype. Finally, we utilized genome-wide shRNA screening to identify molecular targets crucial for cell growth in a selected subtype, which linked the subtype with tubulin polymerization inhibitory drugs.

RESULTS

Molecular heterogeneity of epithelial ovarian cancer

We used a large collection of ovarian tumour gene expression data ($n = 1538$; serous: 1335, mucinous: 27, clear cell: 25, endometrioid: 96, and others: 55 samples; note that the histological distribution is largely biased toward serous adenocarcinoma as opposed to typical clinical setting) derived from 16 independent studies (Supporting Information Table 1) (Anglesio et al, 2008; Bild et al, 2006; Bowen et al, 2009; Denkert et al, 2009; Hendrix et al, 2006; Hogdall et al, 2003; Hsu et al, 2007; Iorio et al, 2010; Jochumsen et al, 2007, 2009; Mok et al, 2009; Pejovic et al, 2009; The Cancer Genome Atlas Research Network, 2011; Tone et al, 2008; Tothill et al, 2008; Tung et al, 2009). Among the 16 datasets, the dataset from TCGA was the largest in sample number ($n = 406$; 26.4% of all samples). All publicly available datasets were included at the time of the study (April 2010), and compiled with an Oslo cohort dataset (BD and JMN). A strong batch-effect was removed by ComBat, eliminating technical differences across data collection sites, while conserving meaningful variations (Supporting Information Fig 1A and B) (Chen et al, 2011; Johnson et al, 2007). A preliminary statistical power analysis showed that 1500 or more samples were required to achieve sufficient statistical power (≥ 0.8) in capturing the complexity and dynamicity of EOC (Supporting Information Fig 2; Supporting Information Materials and Methods) (Fox & Mathers, 1997). In this collection, known prognostic factors were correlated with patient overall survival by univariate and multivariate Cox proportional hazards analyses (Table 1).

To identify EOC molecular subtypes, we applied consensus clustering (CC) to the collection and detected five clusters (Fig 1A) that were characterized by markers of differentiation or cell-type status and stromal components, including the presence of infiltrated inflammatory cells (Supporting Information Table 2). Subtypes were annotated by applying single sample gene set enrichment analysis (ss-GSEA) (Verhaak et al, 2010) with literature-curated gene signatures for epithelial, mesenchymal and stem cells (Supporting Information Text), and confirmed this characterization with the use of appropriate markers. The silhouette plot and SigClust (Liu et al, 2008b) analysis confirmed tumour similarity within each subtype, indicating the robustness of the classification (Supporting Information Fig 3A). The subtype distribution by cohorts and histology is presented in the Supporting Information Text and Supporting Information Figs 4A and B. Subtype distribution within the samples, taken by laser capture microscopy (GSE10971, GSE14407 and GSE18520), implied that the subtypes were intrinsic to cancer cells, and not dependent on stromal cells (Supporting Information Text).

We compared our subgrouping with a previous classification (285 samples; GSE9891) included in our combined dataset (Tothill et al, 2008). An overall concordance of 82.9% for all of the subtypes was found (Supporting Information Table 3; Supporting Information Fig 3B); thus, our large-scale analysis confirmed the previous study, and provided finer distinctions not detectable with fewer samples. Also, we noted that the proposed molecular subtypes were akin to that of serous ovarian carcinoma as proposed by The Cancer Genome Atlas Research Network (2011) (Supporting Information Fig 3B). However, the subtyping schemes from the previous studies did not show a one-to-one match with our proposed classification (Supporting Information Table 3; Supporting Information Fig 3B; Supporting Information Text; see the mutual relationships among Epi-A or Epi-B/C2, C3 or C4/Immunoreactive or Differentiated). This discrepancy may suggest a shared biological feature across these subgroups and hence may cause an imperfect distinction among the subtypes with predictive models as described later (Fig 1D; Supporting Information Fig 8C; Supporting Information Table 8; Supporting Information Text). We also noted that TCGA molecular subtyping did not include a Stem-B/C6 population (Supporting Information Fig 3B; Supporting Information Text). The proposed subtypes in the current study are similar to the previously identified molecular subtypes yet reveal novel biological features.

Correlation of subtype with clinicopathological parameters

We correlated the subtypes with various clinicopathological parameters to ascertain their clinical relevance (Supporting Information Fig 6A; Supporting Information Tables 4A and B; note that the clinicopathological information obtained with each dataset was neither standardized nor centrally reviewed across the datasets; therefore, there might be misdiagnosed or mis-evaluated samples included). We found a significant correlation between subtype and patient outcome: Epi-A, Epi-B and Stem-B subtypes had a better prognosis in a Kaplan–Meier analysis (Fig 1B), while Mes and Stem-A tumours were linked with poorer outcomes. The Mes subtype included more advanced staged and metastasized tumours (Supporting Information Fig 6A; Supporting Information Tables 4A and B), whereas some Stem-A tumours were already found to be at stages 1 and 2 (Supporting Information Fig 6B), with poorer outcomes than those of other subtypes, even at stages 1 and 2 (Supporting Information Fig 6B), Furthermore, Stem-A tumours were enriched in older patients (Supporting Information Fig 6A; Supporting Information Tables 4A and B). The Stem-B subtype, on the other hand, was characterized by multiple histological types, including the majority of mucinous, endometrioid and clear cell carcinoma and some serous carcinoma (Supporting Information Figs 4B, 5 and 6A; Supporting Information Tables 4A and B). Focusing solely on serous tumours (Supporting Information Fig 6D), the frequency of Epi-A-classified tumours decreased significantly as tumour classification moved from serous tumours with low malignant potential (LMP) through to high-grade tumours, whereas the opposite shift in pattern was true for Mes and Stem-A serous tumours. All subtypes displayed high-grade serous carcinoma, with distinctions in survival in Kaplan–Meier curves (Supporting Information Fig 6C). The effect of molecular subtyping on prognosis was significant in both the univariate and multivariate Cox regression analyses with multiple combinations of clinically relevant parameters and status (Table 1; Supporting Information Tables 5A–E; Supporting Information Text).

Clear distinctions were also observed in the enrichment of the gene expression signatures for various pathways. The ss-GSEA analysis of 1538 samples using 6898 gene sets (GSEA databases Supporting Information Table 6) revealed a subtype-specific enrichment of 207 gene sets (Fig 1C; Supporting Information Table 7) (Subramanian & Simon, 2011). Mes tumours correlated with *Metastases* and *TGF-β-related* pathways, consistent with

Table 1. Univariate and multivariate Cox proportional hazards regression analysis for multiple clinical variables and tumour subtypes.

Clinical variables	Sample size (total $n = 539$)	Univariate (HR, 95% CI)	*p*-value	Multivariate (HR, 95% CI)	*p*-value
Age (year)					
<55	175 (32.47%)	1		1	
≥55	364 (67.53%)	1.403 (1.071–1.839)	0.0141	1.285 (0.9781–1.687)[a]	0.07173[a]
Stage					
I or II	47 (8.72%)	1		1	
III or IV	492 (91.28%)	3.907 (1.843–8.285)	0.00038	3.429 (1.591–7.389)[a]	0.00165[a]
Grade					
1	17 (3.15%)	1		1	
≥2	522 (96.85%)	2.58 (0.9578–6.949)	0.0608	1.365 (0.494–3.763)[a]	0.54799[a]
Metastasis					
Primary	500 (92.76%)	1		1	
Metastasis	39 (7.24%)	1.349 (0.8323–2.185)	0.224	1.391 (0.854–2.27)[a]	0.1853[a]
Subtype					
Non-Epi-A	483 (89.61%)	1		1	
Epi-A	56 (10.39%)	0.7103 (0.4498–1.122)	0.142	0.9449 (0.5834–1.53)[b]	0.8176[b]
Non-Epi-B	384 (71.24%)	1		1	
Epi-B	155 (28.76%)	0.69 (0.5206–0.9144)	0.0098	0.7347 (0.5532–0.976)[b]	0.033[b]
Non-Mes	361 (66.98%)	1		1	
Mes	178 (33.02%)	1.171 (0.907–1.513)	0.225	1.01 (0.7771–1.324)[b]	0.9164[b]
Non-Stem-A	411 (76.25%)	1		1	
Stem-A	128 (23.75%)	1.417 (1.075–1.868)	0.0135	1.382 (1.045–1.83)[a]	0.0234[a]
Non-Stem-B	517 (95.92%)	1		1	
Stem-B	22 (4.08%)	1.204 (0.6383–2.271)	0.567	1.14 (0.6033–2.149)[b]	0.6886[b]

Epi-A, epithelial-A; Epi-B, epithelial-B; Mes, mesenchymal; Stem-A, stem-like-A; Stem-B, stem-like-B.
p-values below 0.05 are shown in red.
[a] Multivariate Cox regression analysis of clinical variables with Stem-A subtype.
[b] For multivariate Cox regression, each subtype was independently analysed with the other clinical variables (age, stage, grade and metastasis) from the remaining subtypes.

their link with epithelial–mesenchymal transition (EMT) and metastasis (Supporting Information Fig 6A) (Maruyama et al, 2000; Yin et al, 1999). In comparison, *chromatin modification* gene sets were highly enriched in the Stem-A subtype (Fig 1C; Supporting Information Table 7). Overall, this expression-based subtyping scheme dissected ovarian serous carcinoma heterogeneity into subgroups with similar biological properties.

Predictive framework for EOC subtype classification

We next developed a predictive model with BinReg as a potential diagnostic tool for quantitative gene expression-based subgroup assignment (Supporting Information Fig 7A and B) (Gatza et al, 2010). This was performed using microarrays of representative samples for each subtype ($n = 50$ per subtype). Fig 1D shows predicted probabilities for subtype status of the remaining samples ($n = 1413$) not used in building predictive model. A comparison of the subtype predicted by BinReg with that classified by the CC (Fig 1A) revealed an overall 78.8% concordance for all subtypes (78.5% for core samples) (Fig 1D; Supporting Information Table 8), and a highly similar pattern of patient outcomes (Fig 1B; Supporting Information Fig 7C). This demonstrated the powerful predictive capability of the method, with the concordance comparable with those reported in previous studies for multiple breast cancer cohorts (Supporting Information Text) (Calza et al, 2006; Haibe-Kains et al, 2012). We affirmed the accuracy of this method using 10-fold cross-validation (Supporting Information Figs 8A–C) (Blum et al, 1999; Kim, 2009; Konavi, 1995), 3-way split cross-validation (Ewens & Grant, 2001), and also by comparing BinReg to ClaNC (Supporting Information Fig 9; Supporting Information Materials and Methods).

To ensure the robustness of the classifier, we performed validation on five independent ovarian cancer datasets (total $n = 418$; Supporting Information Table 1) (King et al, 2011; Konstantinopoulos et al, 2010; Meyniel et al, 2010) that were not included in the prediction modelling. We observed high concordance for the gene expression patterns and clinicopathological characteristics in the predicted molecular subtype (Fig 1E; Supporting Information Tables 4A, C and D). Using 260 samples from the validation set (GSE19829 [$n = 28$], GSE30311 [$n = 47$] and GSE26712 [$n = 185$]), for which patient outcome information was supplied (Konstantinopoulos et al, 2010), the Kaplan–Meier analysis on the BinReg-predicted molecular subtypes revealed a similar pattern of patient prognoses with that of the original CC analysis ($p = 0.0372$ by the log-rank test; Fig 1B; Supporting Information Fig 7D) for subtypes other than Stem-B (Supporting Information Text). ClaNC (Dabney, 2006; Verhaak et al, 2010) further confirmed the highly comparable and predictive capability of this EOC subtyping (Supporting Information Fig 8D). Thus, the molecular subtype prediction model can assign clinical samples with unknown subtype status with high accuracy.

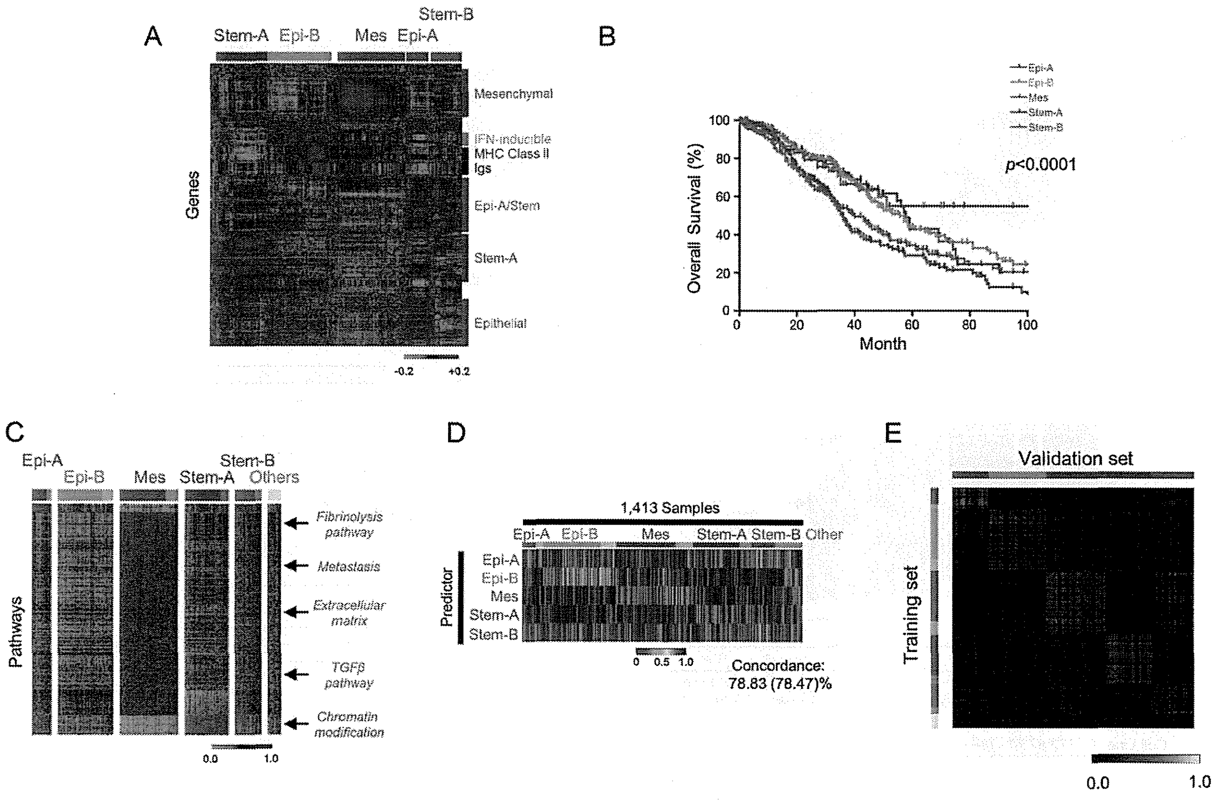

Figure 1. CC analysis revealed five subtypes of epithelial ovarian carcinoma.

A. Gene expression heatmap for the five tumour clusters (red = high; green = low expression). CC of 1538 samples identified five subtypes, designated by the associated gene components. Note the similarities between Epi-A/Stem-B subtype tumours, between Epi-A/Epi-B subtypes for epithelial genes, and the expression pattern of Epi-A/Stem genes. Also note that none of cultured cell-line data was included in this analysis.

B. Kaplan–Meier survival analysis for each subtype. Among data for 1538 patient samples, survival information for 978 samples was available (GSE3149: 143, GSE9891: 277, TCGA: 400, GSE14764: 80, GSE18520: 53 and Oslo cohort: 25 samples) (Epi-A: 80, Epi-B: 264, Mes: 284, Stem-A: 220, Stem-B: 61 and others: 69 samples) and used for the Kaplan–Meier analysis.

C. Subtype-specific pathway enrichment. Heatmap shows subtype-specific single sample gene set enrichment analysis (ss-GSEA) scores (false discovery rate (FDR) in significance analysis of microarrays (SAM) $q = 0\%$, receiver operating characteristic (ROC) >0.85) for 1538 ovarian cancer samples. Red = high; green = low enrichment scores. Gene sets are aligned in descending value of ROC. Samples are aligned by subtype classification and SW. Deep colour = positive SW (core samples); pale colour = samples classified, but negative SW. "Others" indicates the unclassified samples not grouped in any of the five subtypes in the initial CC analysis in Fig 1A. Arrows indicate positions of selected pathways.

D. Ovarian cancer subtype predictors (BinReg). A heatmap is shown for the predicted probabilities of subtype status on 1413 clinical samples not used in the subtype predictor generation. Red = high; blue = low. Samples were aligned according to subtype classification by CC and SW. Colour as for (C). "Others" is represented as for (C).

E. Heatmap of Spearman correlation *Rho* between the subtype of training data ($n = 1538$) and the BinReg predicted subtype of samples in five independent datasets (GSE19829, GSE20565, GSE30311, GSE26712 and GSE27651; total $n = 418$). The validation samples are aligned horizontally according to the predicted subtype, whereas the training samples are aligned vertically according to the subtype. Yellow = high correlation; black = low correlation.

Abbreviations: Epi-A, epithelial-A; Epi-B, epithelial-B; Mes, mesenchymal; Stem-A, stem-like-A; Stem-B, stem-like-B.

Identification of representative cell lines for each subtype

Cell lines corresponding to each EOC subtype were identified for *in vitro* modelling. We performed two rounds of CC on a pool of datasets from 142 cultured EOC cell lines, resulting in Epi-A: 29, Epi-B: 10, Mes: 34, Stem-A: 42 and Stem-B: 27 cell lines (Supporting Information Figs 10A and B); the results were unambiguously supported by similarity matrices, the silhouette values with significant *p*-value by SigClust (Fig 2A) (Liu et al, 2008b), as well as consistent subtype assignments amongst biological replicates of 28 cell lines (Supporting Information Table 9; Supporting Information Text). The cell-line subtype predictors (Fig 2B) were then applied to tumour core samples to estimate the molecular similarity of the subtypes between *in vivo* tumours and *in vitro* cell lines. We observed a high level of accuracy in the *a*rea *u*nder the *c*urve (AUC: 0.744 to 0.918) and a high concordance between the predicted tumour subtype by a cell-line classifier with the initially assigned tumour subtype (75.8–87.9%) (Fig 2B). Furthermore, we found a high

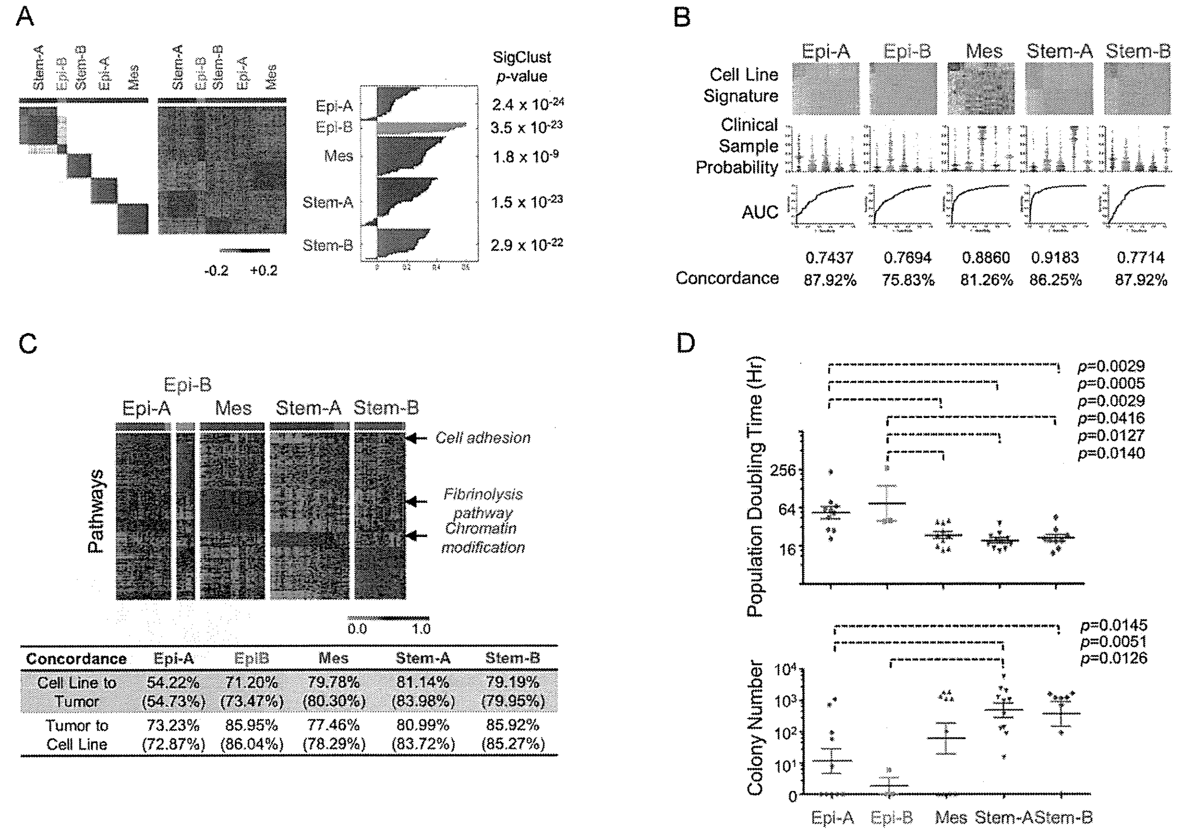

Concordance	Epi-A	EpiB	Mes	Stem-A	Stem-B
Cell Line to Tumor	54.22% (54.73%)	71.20% (73.47%)	79.78% (80.30%)	81.14% (83.98%)	79.19% (79.95%)
Tumor to Cell Line	73.23% (72.87%)	85.95% (86.04%)	77.46% (78.29%)	80.99% (83.72%)	85.92% (85.27%)

Figure 2. Identification of cell line subtype status.

A. Five subtypes in ovarian cancer cell line classification. Left panel. CC matrix of 142 ovarian cell lines. Red = high; white = low similarity. Middle panel. Gene expression heatmap of ovarian cell lines. Red = high; green = low expression. Right panel. Silhouette analysis for each subtype. Column to the right of silhouette plot is the SigClust (Liu et al, 2008b) *p*-value indicative of cluster significance for each subtype.

B. Prediction of clinical samples by cell line predictors using BinReg. Upper panel. Gene expression heatmaps for subtype predictors based on cell line expression data. Red = high; blue = low expression. Middle panel. Predicted probability of core clinical samples for cell-line subtype predictor by BinReg. Each subtype signature detected the probability difference between the corresponding subtype from the remaining subtypes with statistical significance ($p < 0.0001$; Mann–Whitney *U*-test). Lower panel. Receiver operating characteristic (ROC) analyses of subtype predictors. Overall accuracy is shown by the area under the ROC curve (AUC) (Pejovic et al, 2009). Concordance (%) of the subtype status derived from CC with the prediction based on the cell line subtype predictors.

C. Upper panel. Cell line subtype-specific pathway enrichment. Subtype-specific single sample gene set enrichment analysis (ss-GSEA) scores (false discovery rate (FDR) of the significance analysis of microarrays (SAM) $q = 0\%$, ROC > 0.85 as overexpressed gene sets) for 142 ovarian cell lines are shown as a heatmap. Red = high; green = low enrichment scores. Gene sets aligned in descending value of ROC; samples are aligned according to the subtype classification by CC and the SW. Deep colour = positive SW (core samples); pale colour = samples classified to a subtype, but negative SW. Arrows indicate positions of selected pathways. Lower panel: Concordance (%) of the subtype status (from CC by genes) with the prediction result (from BinReg based on the subtype predictors by enrichment scores). The number in parentheses indicates the accuracy of the prediction against core samples.

D. Characterization of *in vitro* phenotypes of cell lines in each subtype. Upper panel. Population doubling time of a cell line was measured with the MTS assay (Matsumura et al, 2011) and is shown as dot plots. Lower panel. Anchorage-independent cell growth ability for each cell line was measured using the methylcellulose assay (Mori et al, 2009). Log_{10}-transformed colony number is shown. *p*-values were computed by Mann–Whitney *U*-test. Abbreviations: Epi-A, epithelial-A; Epi-B, epithelial-B; Mes, mesenchymal; Stem-A, stem-like-A; Stem-B, stem-like-B.

correlation between clinical tumour subtype and cell line subtype in the Spearman correlation map analysis (Supporting Information Fig 10C). These findings indicated a high level of similarity between ovarian cancer cell lines and tumour transcriptomic expression patterns (Fig 2B; Supporting Information Fig 10C).

We next compared the pathway activation for these 142 cell lines with that of the clinical tumours using ss-GSEA analysis (Figs 1C and 2C; Supporting Information Table 10). Epi-A cell lines were characterized by cell adhesion-related gene sets, reflecting enrichment of epithelial cell markers. Importantly, 33 of the 402 cell line subtype-specific gene sets were shared with tumours, including enrichment of *fibrinolysis pathway* and *chromatin modification* in the Mes and Stem-A subtypes, respectively (Supporting Information Table 10); this was confirmed with BinReg analyses using a statistical model with